BisDeNet: A New Lightweight Deep Learning-Based Framework for Efficient Landslide Detection

Tao Chen, *Senior Member, IEEE*, Xiao Gao, Gang Liu, Chen Wang, Zeyang Zhao, Jie Dou, Ruiqing Niu, and Antonio J. Plaza, *Fellow, IEEE*

***Abstract*—Landslides are catastrophic geological events that can cause significant damage to properties and result in the loss of human lives. Deep-learning technology applied to optical remote sensing images can enable effective landslide-prone area detection. However, conventional landslide detection (LD) models often employ complex structural designs to ensure detection accuracy. The complexity often hampers the detection speed, rendering these models inadequate for the swift emergency monitoring of landslides. To address these problems, we propose a new lightweight deep-learning-based framework, BisDeNet, for efficient LD. To improve the efficiency of the proposed BisDeNet, we replaced the context path in the original BiSeNet with DenseNet due to its strong feature extraction ability, few required parameters, and low model complexity. Two sites with different and representative landslide developments were selected as the study areas to verify the performance of our proposed BisDeNet. Additionally, we introduced landslide causative factors to enhance the sampling dataset. To evaluate the effectiveness of our approach, we compared the performance of our BisDeNet with the performances of three other BiSeNet-based methods and an advanced transformer-based model data-efficient image transformer (DeiT). Our experimental results indicate that the *F*1-scores of BisDeNet in the two study areas are 0.9006 and 0.8850, which are 26.22% and 1.86% higher than the scores of BiSeNet, respectively, but slightly lower than that of the DeiT model. Furthermore, our proposed BisDeNet requires the fewest number of parameters and the least memory out of the five models.**

***Index Terms*—Bilateral segmentation network (BiSeNet), DenseNet, landslide detection (LD), lightweight model, remote sensing (RS).**

Manuscript received 13 September 2023; revised 11 December 2023 and 22 December 2023; accepted 6 January 2024. Date of publication 9 January 2024; date of current version 29 January 2024. This work was supported in part by the National Natural Science Foundation of China under Grant 62371430 and Grant 62071439, in part by the Opening Fund of State Key Laboratory of Geohazard Prevention and Geoenvironment Protection, Chengdu University of Technology under Grant SKLGP2022K016, in part by the Open Fund of State Key Laboratory of Remote Sensing Science under Grant OFSLRSS202207, in part by the Open Fund of Badong National Observation and Research Station of Geohazards under Grant BNORSG-202302, in part by the Opening Fund of the Key Laboratory of National Geographic Census and Monitoring, Ministry of Natural Resources under Grant 2023NGCM11, and in part by the Open Fund of Hebei Cangzhou Groundwater and Land Subsidence National Observation and Research Station under Grant CGLOS-2023-02. *(Corresponding authors: Tao Chen; Gang Liu.)*

Tao Chen is with the School of Geophysics and Geomatics, China University of Geosciences, Wuhan 430074, China, also with the Badong National Observation and Research Station of Geohazards, China University of Geosciences, Wuhan 430074, China, also with the Key Laboratory of National Geographic Census and Monitoring, Ministry of Natural Resources, Wuhan 430079, China, and also with the State Key Laboratory of Geohazard Prevention and Geoenvironment Protection, Chengdu University of Technology, Chengdu 610059, China (e-mail: taochen@cug.edu.cn).

Xiao Gao is with the School of Geophysics and Geomatics, China University of Geosciences, Wuhan 430074, China, also with the College of Surveying and Geo-Informatics, Tongji University, Shanghai 200092, China, and also with the Center for Spatial Information Science and Sustainable Development Applications, Tongji University, Shanghai 200092, China (e-mail: gaoxiao@cug.edu.cn).

Gang Liu is with the State Key Laboratory of Geohazard Prevention and Geoenvironment Protection, Chengdu University of Technology, Chengdu 610059, China (e-mail: liuganggis@sina.com).

Chen Wang, Zeyang Zhao, and Ruiqing Niu are with the School of Geophysics and Geomatics, China University of Geosciences, Wuhan 430074, China (e-mail: eurydice@cug.edu.cn; zhaozy@cug.edu.cn; niuruiqing@cug.edu.cn).

Jie Dou is with the Badong National Observation and Research Station of Geohazards, China University of Geosciences, Wuhan 430074, China (e-mail: doujie@cug.edu.cn).

Antonio J. Plaza is with Hyperspectral Computing Laboratory, Department of Technology of Computers and Communications, Escuela Politécnica, University of Extremadura, 10071 Cáceres, Spain (e-mail: aplaza@unex.es).

Digital Object Identifier 10.1109/JSTARS.2024.3351873

I. Introduction

LANDSLIDES are disasters caused by the sliding of rock masses or soil along one or more rupture slip surfaces under gravity. Landslides occur suddenly, are large in quantity, and are greatly harmful [1]. Landslide detection (LD) is very important for recording the occurrence range, size, and distribution of landslides in disaster areas, studying and investigating the recurrence and statistics of landslides, determining vulnerability to landslides and the danger and risk of landslides occurring, and also for studying the evolution of topography and geomorphology [2].

With the development of Earth observation technology and digital image processing technology, disaster emergency monitoring has been swiftly combined with remote sensing (RS) technology [3]. RS enables comprehensive surface information to be rapidly acquired, greatly enhancing the convenience and efficiency of information gathering. Furthermore, through sophisticated processing of remote sensing images (RSIs), various environmental parameters, such as vegetation index, water body index, land use, elevation, slope, aspect, and curvature, can be accurately derived, providing valuable insights into the overall ecological landscapes. The availability of abundant RSIs with high temporal, spatial, and spectral resolutions has revolutionized the field of RS applications [4]. Consequently, image classification algorithms are being increasingly harnessed for LD. These algorithms leverage the unique reflectivity variations and spectrum information found among different objects within RSIs, enabling areas susceptible to landslides to be accurately

identified and effectively distinguished from nonlandslide areas. Combining advanced algorithms with high-quality RSIs enables enhanced precision and efficacy in landslide monitoring and assessment. This empowers stakeholders to make informed decisions, implement targeted mitigation measures, and develop comprehensive disaster management strategies [5], [6], [7]. In general, landslide areas exhibit high reflectivity in RSIs, which allows to distinguish these areas from features with low reflectivity. However, this characteristic can also lead to landslide areas being confused with bare land, as bare land can also exhibit high reflectivity. Moreover, the traditional pixel-oriented methods primarily focus on individual pixel characteristics and do not account for the spatial structures and relationships with other attribute features, such as shape and texture. These limitations often cause classification results that suffer from "salt and pepper" noise, compromising their accuracy and reliability. These challenges have been commonly addressed by traditional methods, such as maximum likelihood, support vector machines, decision trees, and random forest algorithms. These approaches aim to improve classification by considering additional contextual information and multiple attributes, thereby enhancing the robustness and precision of LD in RSIs [8], [9], [10]. In recent years, high-resolution sensors have been increasingly deployed on Earth observation satellites, significantly enriching the available research data. Consequently, a new approach to image analysis based on landslide objects has emerged [11]. This method leverages various information from RSIs, including spectrum, shape, texture, context semantics, and topography, to extract comprehensive ground object information for analysis and judgment, ultimately facilitating LD [12]. However, object-oriented recognition methods typically rely on image segmentation algorithms, and the segmentation scale has a critical impact on the recognition results. Often, the segmentation scale is chosen based on the texture features of the image. Unfortunately, some existing image segmentation algorithms struggle to handle complex large-scale RS data, resulting in inefficient LD and posing challenges for improving performance [13].

In recent years, the rapid advancement of deep-learning (DL) algorithms has propelled convolutional neural networks (CNNs) to the forefront as mainstream methods. Compared with traditional approaches, CNNs exhibit remarkable feature learning capabilities through convolution operations, surpassing empirical feature design methods in various image-based tasks, such as image classification [14], semantic segmentation [15], and target detection, and yielding significant achievements. However, the application of CNNs for RS-based LD is still nascent [16], [17], [18].

In some studies, CNNs have been utilized for RS image analysis in LD. For instance, in [19], CNNs were employed to extract features from pre- and postlandslide RSIs, and landslide occurrences were determined by calculating the Euclidean distance between the two feature vectors. In [20], a simple convolutional network was trained to retrieve landslides from test images, and a region growth algorithm was applied to extract discriminant regions, boundaries, and centers of the landslides. In [21], the impact of the number of convolution layers, size of convolution kernels, and number of input data channels on LD were investigated. In these studies, relatively simple and basic neural network (NN) architectures were primarily employed. These architectures comprise multiple convolutional and pooling layers for extracting landslide features, followed by fully connected layers for LD. However, there is a growing research trend toward replacing fully connected layers with 1×1 convolutional layers and constructing target detection networks for end-to-end image classification and recognition of LD. For example, in [22], FCN-PP was proposed by integrating the pyramid pooling (PP) module with a fully convolutional network (FCN). This approach effectively incorporated the characteristics of multiple convolutional layers and explored the contextual information of the images, balancing the broader acceptance domain and context utilization, thereby improving the landslide surveying and mapping effectiveness. In [23], a susceptibility-guided LD model based on FCN was proposed, incorporating landslide susceptibility as *a priori* knowledge. In [24], residual modules were introduced to the U-Net semantic segmentation network, enabling landslides to be rapidly identified after the Jiuzhaigou earthquake and facilitating swift responses and decision making. In [25], a lightweight attention U-Net based on the light detection and ranging data was proposed for automatic detection of historical landslides. In [26], an attention module was added to UNet++, which used RegNet instead of convolutional blocks in the encoder to improve the LD accuracy. In [27] and [28], feature fusion modules (FFMs) were proposed to realize the fusion of different features to improve the accuracy of semantic segmentation models, respectively. In [29], the LandsNet semantic segmentation network was enhanced to intelligently detect and delineate earthquake-induced landslides from single-phase RapidEye RSIs. This method exhibited high accuracy and significant potential for emergency response to natural disasters. In [30], generative adversarial networks (GANs) were employed in a twin NN framework, and the GAN-based Siamese framework was proposed. This framework directly generated landslide inventory maps without any preprocessing or postprocessing steps, yielding promising results. In [31], experiments were conducted using RapidEye images and machine learning models in the Himalayan region of Nepal, with the U-Net model performing optimally when appropriately sized patches were selected. Additionally, including digital elevation model (DEM) data improved the LD performance.

Most of the aforementioned semantic segmentation networks are U-shaped structures composed of encoders and decoders. Considering that this network structure greatly reduces the model training speed, the information lost in the pooling process cannot always be passed through simple upsampling and fusion layers for restoration. In [32], a bilateral segmentation network (BiSeNet) was proposed in 2018. A spatial path (SP) with a step size of 2 was designed to preserve the spatial position information, and a semantic path with fast downsampling was designed to obtain objective receptive fields. A special FFM was introduced between these two modules to effectively fuse the feature maps of the two paths, balancing model efficiency and segmentation accuracy.

With the continuous improvement of computing power, DL has achieved great success in the computer vision field, and

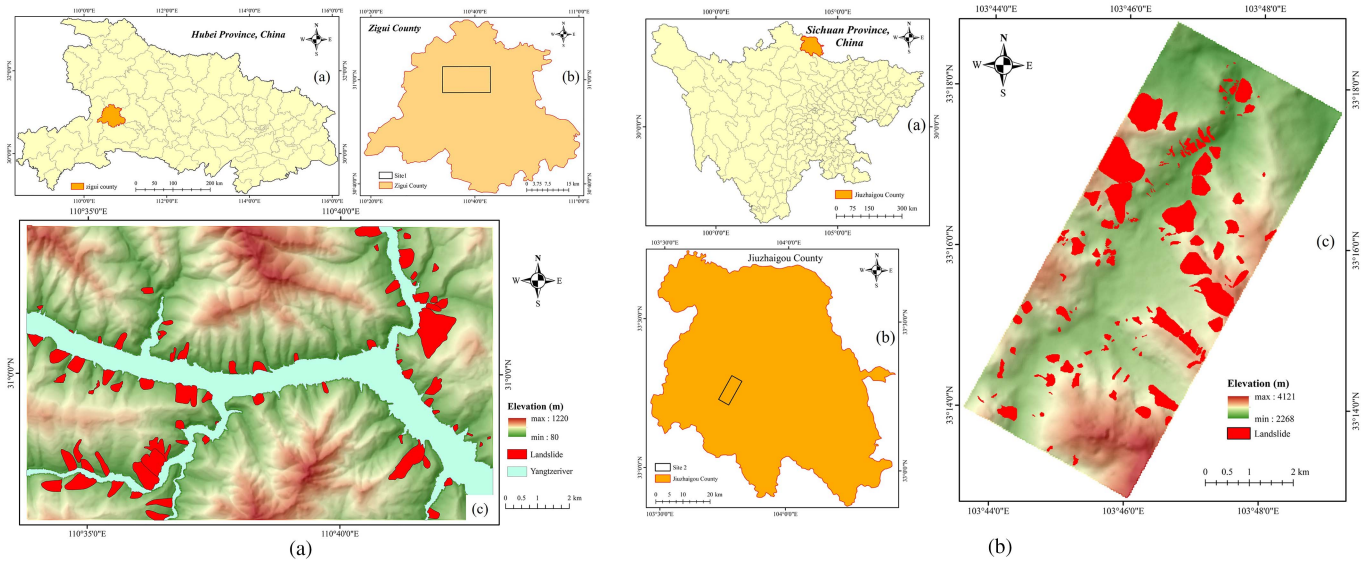

Fig. 1. Location of the study areas. (a) Site 1: Zigui county. (b) Site 2: Jiuzhaigou county.

image semantic segmentation methods based on CNNs have achieved significant development. However, further improving segmentation algorithm efficiency while maintaining accuracy is still a major problem in this field. LD typically necessitates the consideration of both surface details and broader contextual information. BiSeNet employs a multiscale information fusion strategy, contributing to a more comprehensive understanding of surface conditions and enhancing its capability to discern landslide-prone areas. Given that landslides often present complex shapes and textures, the bilateral convolutional structure of BiSeNet proves instrumental in capturing these intricate surface features, thereby improving accuracy in LD. Moreover, due to its lightweight design, BiSeNet is well suited for operation in resource-constrained environments, such as embedded systems and mobile devices, making it more feasible for practical applications in LD.

To address the above issues, in this article, we develop a new lightweight-based DL framework, BisDeNet, for efficient LD. The main contributions of our work can be summarized as follows: First, we introduce a new lightweight-based DL framework for efficient LD, BisDeNet, with strong feature extraction ability, few parameters, and low model complexity; second, the proposed BisDeNet is applied to LD in two different landslide-prone areas, improving the LD accuracy and efficiency of the framework.

The rest of this article is organized as follows. Section II comprehensively introduces the study areas and overviews the datasets employed in the experiments. Section III outlines the experimental steps undertaken to develop the new framework. Section IV analyzes the experimental results in detail, presenting both qualitative and quantitative findings. Section V discusses the model's complexity, the significance of influencing factors, the limitations inherent to this study, and future research prospects. Finally, Section VI concludes this article.

II. Study Area and Data

A. Study Area

To verify the performance of the proposed method, two typical regions with severe landslide disasters were selected for experimentation: Zigui County in Hubei Province and Jiuzhaigou County in Sichuan Province, China (see Fig. 1). These two areas are characterized by diverse environmental backgrounds, complex geological conditions, and active tectonic activity. However, the causes and development characteristics of landslides differ, making these areas representative and typical. They are, thus, sufficient for demonstrating the generalizability of the proposed method.

1) Site 1—Zigui County: Site 1 is located in Zigui County, Hubei Province. This site has a latitude range of 30°57'–31°02' N and a longitude range of 110°33'–110°42' E, covering a total area of 135 km^2 [see Fig. 1(a)]. This site is in a subtropical monsoon climate region. Due to the influence of monsoons, the rainy season in this site occurs from May to September each year. The majority of annual rainfall, 70% of the total annual precipitation, is concentrated within these five months. The climate characteristics of abundant rainfall, high humidity, and frequent heavy rain make the research area prone to landslide disasters. The elevation in the area ranges from 80 to 1220 m. Furthermore, the topography and geomorphological structure of the research area are quite complex, consisting mainly of mountainous regions with a variety of rock types and highly unstable geological structures. These unstable geological structures often lead to various geological hazards, particularly landslide disasters. In addition, the rapid economic development in the research area in recent years has been accompanied by large-scale human engineering activities. Activities, such as population migration, the construction of the Three Gorges Reservoir, deforestation, and mineral exploitation, have greatly increased the risks of

slope instability and subsequent landslide disasters. In summary, due to its unique geographical environment, Site 1 is inevitably at risk of various geological hazards, especially landslides [11], [33]. The image size of Site 1 is 616 × 976 pixels with a spatial resolution of 15 m.

2) Site 2—Jiuzhaigou County: The study area of Site 2 is located in Jiuzhaigou County, Aba Tibetan, and Qiang Autonomous Prefecture, Sichuan Province, China. As shown in Fig. 1(b), this site lies in the transitional zone between the western edge of the Sichuan Basin and the Qinghai–Tibet Plateau, with an approximate longitude range of 103°43′ E to 103°49′ E and an approximate latitude range of 33°12′ N to 33°18′ N, encompassing a total area of 96 km^2. The elevation within this area varies from 2268 to 4121 m. The elevation gradually increases from south to north, and the terrain features deep-cut valleys and significant altitude differences. Site 2 has a complex geological background, with a widespread distribution of carbonate rocks, extensive folding and faulting, intense tectonic activity, and substantial crustal uplift, resulting in various landforms. On August 8, 2017, a magnitude 7.0 earthquake occurred in this region, with the epicenter near Zhangzha Town in Jiuzhaigou County. The earthquake was situated near the Minjiang Fault, Tazang Fault, and Huya Fault at coordinates 33.20° N latitude and 103.82° E longitude, with a focal depth of 20 km. The earthquake caused significant life and property losses for the local population and tourists. Statistics indicated that the earthquake resulted in a total of 31 deaths or disappearances and 525 injuries. It also affected nearly 20 000 people, damaged over 70 000 houses, and triggered over 4800 landslides [34], [35]. The image size of Site 2 is 733 × 585 pixels with the same spatial resolution as the Site 1 image.

B. Landslide Inventory

The landslide inventory maps for Site 1 and Site 2 were created after conducting field surveys and interpreting images using Google Earth. After the field surveys, 74 landslides covering an area of 6.82 km^2 in Site 1 were mapped, accounting for 5.05% of the Site 1 area, and 124 landslides covering an area of 6.08 km^2 were mapped in Site 2, accounting for 6.33% of the total Site 2 area. The landslides in these two study sites were then digitized and rasterized using Environmental Systems Research Institute ArcGIS software (version 10.3.0). The spatial resolution used for this process was 15 m.

C. Landslide Causative Factors (LCFs)

Predicting the correlation between landslide occurrence and various LCFs has proven to be challenging due to the complex nature and evolution of landslides [16], [17], [18], [36], [37], [38], [39], [40], [41], [42], [43], [44]. In this study, the causes and distributions of landslides across different study areas, along with their local topographical features, were accounted for. Various LCFs were selected to improve landslide feature learning and enhance the LD accuracy. Based on the previous studies [45], the following nine LCFs were chosen as input data: elevation, slope, aspect, curvature, normalized difference vegetation index (NDVI), modified normalized difference water index (MNDWI), distance to river (DTR), distance to fault (DTF), and lithology of the two sites. Four topographic factors, including elevation, aspect, slope, and curvature, for both sides were generated from a DEM. The lithology and DTF factors were derived from the lithology map at a 1:50000 scale for Site 1 and a 1:200000 scale for Site 2. The NDVI and MNDWI maps were prepared based on Landsat 8 OLI data, with acquisition dates of 2013/09/15 for Site 1 and 2018/04/09 for Site 2. The DTR maps for both sites were derived from the topographical map by buffering the river lines. Table I presents the detailed information about the LCFs of the two sites.

TABLE I
DETAILED VALUES OF LCFS IN TWO SITES

LCFs	Values	
	Site 1	Site 2
Elevation (m)	[80, 1220]	[2068, 4121]
Aspect	Flat, North, Northeast, East, Southeast, South, Southwest, West, Northwest	
Slope (°)	[0, 62.69]	[0, 67.57]
Curvature (°/100m)	[−7.85, 5.47]	[−6.33, 5.67]
Lithology	Soft rock, Alternating soft and hard rock, Hard rock	
DTF (m)	[0, 8754]	[0, 6860]
NDVI	[−0.60, 0.68]	[−0.08, 0.29]
MNDWI	[0.45, 0.99]	[0.35, 0.99]
DTR (m)	[0, 3063]	[160, 3032]

III. METHODOLOGY

The proposed BisDeNet framework consists of three main parts, as illustrated in Fig. 2. The first part focuses on data preprocessing and creating the training dataset specifically designed for BisDeNet. This stage involves optical image processing, sample annotation, and LCF extraction, generating sample sets through standardization and cropping operations. The second part of the framework utilizes the BisDeNet algorithm. This is the first time that a lightweight BiSeNet has been used to effectively detect and identify landslides. Finally, model evaluation is conducted in the third part of the framework. Several evaluation metrics (EMs) are employed to compare the performance of our proposed BisDeNet framework to the performances of three other BiSeNet-based methods, including the original BiSeNet [32].

A. Data Preprocessing

The data preprocessing in this study encompassed several key steps: resampling, image standardization, pixel patch generation, and data augmentation. The Landsat 8 OLI data and LCF data of the two study sites were initially cropped based on selected vector ranges. Given the varying resolutions of different data types, resampling was performed based on the bilinear interpolation method to ensure consistent row and column numbers [46]. Next, all the input data were normalized based on the Z-score method to facilitate DL network training. Each channel of the input data was normalized to achieve a

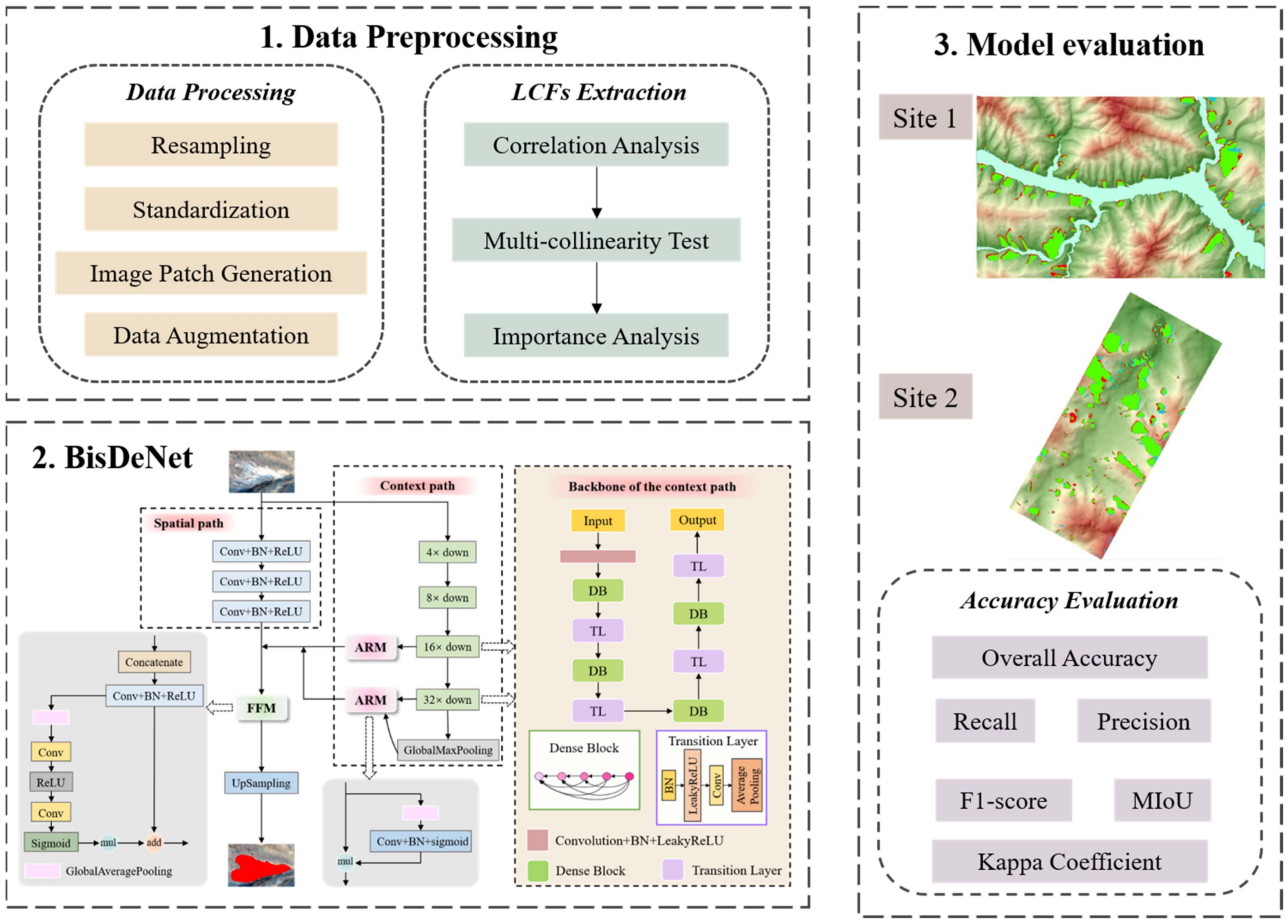

Fig. 2. Framework of BisDeNet-based LD method.

uniform data distribution with a mean of 0 and a variance of 1. This normalization can align data distributions across different dimensions and accelerate model convergence [47]. Finally, the processed layers were organized into blocks of size $m \times n \times c$ and fed into the DL network for training, where m and n denote the number of rows and columns, respectively, and c represents the number of channels.

Although DL exhibits significant advantages for landslide-related research [32], [48], it typically requires many training samples. However, even representative high-quality training samples have inherent deficiencies. Furthermore, in natural settings, the ratio of landslide to nonlandslide instances is severely imbalanced. This issue is particularly pronounced in RS-based LD [49], [50]. Drawing inspiration from pioneering research in the field, a data augmentation strategy is employed to generate additional training samples in this work [51], [52]. To enhance the proportion of positive samples, such as landslides, landslide points were randomly selected as seed pixels within the training area.

B. LCFs Selection

The factor selection process has a crucial impact on the overall model performance. On the one hand, a significant amount of noise (such as factors with very low or zero contribution rates in the dataset) impacts the model's prediction results, leading the true landslide characteristics to be inadequately learned. On the other hand, strong correlations among the factors can result in data redundancy, reducing the model's efficiency and influencing the allocation of feature weights during the learning process [53]. Therefore, in this study, correlation analysis, collinearity testing, and importance evaluation were conducted on the landslide factors before constructing the landslide sample datasets.

1) Correlation Analysis: The Pearson correlation coefficient (PCC) was used to characterize the correlations between pairwise selected LFCs [54]. The PCC value ranges between -1 and 1. A positive PCC indicates a positive correlation, whereas a negative PCC indicates a negative correlation. A PCC value close to 1 or -1 indicates a strong linear relationship, while a PCC value of 0 implies that no linear relationship exists between the variables. The PCC is calculated as follows:

$$\begin{aligned} \mathrm{PCC} &= \frac{\operatorname{cov}(X,Y)}{\sigma_X \sigma_Y} \\ &= \frac{\sum_{i=1}^{n}\left(X_i-\bar{X}\right)\left(Y_i-\bar{Y}\right)}{\sqrt{\sum_{i=1}^{n}\left(X_i-\bar{X}\right)^2}\sqrt{\sum_{i=1}^{n}\left(Y_i-\bar{Y}\right)^2}} \end{aligned} \tag{1}$$

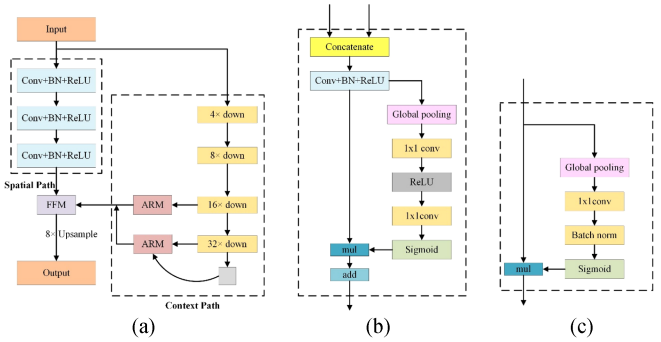

Fig. 3. Network structure of the BiSeNet. (a) BiSeNet architecture. (b) FFM. (c) Attention refinement module (ARM).

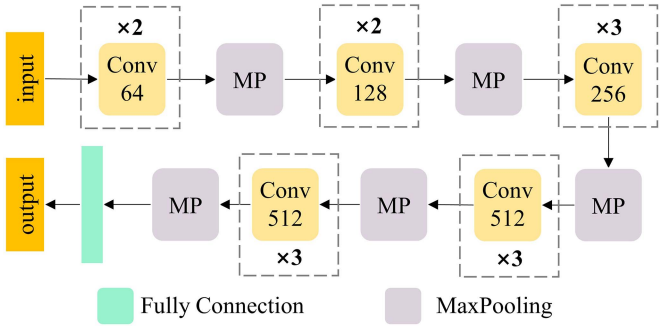

Fig. 4. Network structure of the VGG16.

where n represents the total number of samples and σ_X and $\overleftarrow{X}$ are the sample standard deviation and sample mean of the samples X_i, respectively. Similarly, σ_Y and $\overleftarrow{Y}$ are the sample standard deviation and sample mean of the samples Y_i, respectively. $\mathrm{cov}(X, Y)$ represents the covariance between the samples X_i and Y_i.

2) Multicollinearity Test: A multicollinearity analysis was conducted to further evaluate the correlations between LCFs. Multicollinearity refers to the condition in linear regression models where explanatory variables are highly or precisely correlation, leading to distorted or unreliable model estimates [55]. In this study, SPSS Statistics software was used to compute the variance inflation factor (VIF) and tolerance (TOL) for each factor.

The VIF is calculated by

$$\mathrm{VIF} = \frac{1}{1 - R_i^2}. \tag{2}$$

We defined $X = \{X, X_2, \ldots, X_N\}$ as an independent variable dataset. R_i^2 represents the coefficient of determination when the ith independent variable X_i is regressed on all other predictor variables in the model. TOL, on the other hand, is the reciprocal of the VIF. Generally, a factor should be removed when its VIF exceeds 10 or 5.

3) Importance Evaluation: To verify the impact of each LCF on the model's performance, we conducted an importance evaluation of the nine LCFs in the two study areas before modeling. In this study, we used the Gini index in the random forest model to rank the importance of the LCFs [56]. Ultimately, each study area generated a 1×9 array, in which each element had a positive value and the sum of these values was equal to 1. The higher the value of an element is, the greater the corresponding LCFs contribution to the model.

C. BiSeNet

BiSeNet has been proven to efficiently extract features, including the SP and the contextual path (CP) [32]. The network structure of BiSeNet is shown in Fig. 3. The SP addresses spatial information loss in deep networks by capturing more low-level features. It focuses on low-level information and consists of three convolutional layers, each containing a convolutional layer with a stride of 2. After batch normalization and ReLU nonlinear activation, the output feature size becomes one-eighth the size of the input image, and rich spatial detail information is encoded. The CP module enables the network to obtain a larger receptive field. In the CP, the attention refinement module (ARM) aggregates features from different depths and further processes high-level features. Given features at different levels, the FFM connects the output features of the SP and CP. The connected features are then pooled into a feature vector, and a weight vector is calculated to effectively reweight and combine the features from the SP and CP. The network used in the CP in BiSeNet is the Xception model [32].

D. BiSeNet-VGG

The VGG network explores the relationship between the depth of CNNs and their performance [57]. It exhibits similar feature extraction capabilities as other networks by reducing the size of the convolutional kernels and increasing the number of convolutional layers. The VGG network uses consecutive small convolutional kernels (3×3) and pooling layers to construct a deep NN. The network depth can reach 16 layers or 19 layers. It is composed of multiple alternating convolutional layers and pooling layers, followed by fully connected layers for classification. In this article, the CP is replaced by VGG16 because VGG16 is one of the most widely used VGG networks. The VGG network architecture is shown in Fig. 4.

E. BiSeNet-ResNet

The main feature of ResNet is the introduction of residual blocks to address vanishing and exploding gradients in deep CNNs [50]. In a residual block, a shortcut connection allows the input to be directly connected to the output, enabling the network to learn residual information and improve feature extraction and processing. ResNet18 consists of 18 layers with weights, and it effectively addresses degradation by allowing deep-layer gradients to flow directly back to shallow layers. Therefore, in this article, the original semantic path of BiSeNet is replaced by ResNet18. The ResNet18 network architecture is shown in Fig. 5.

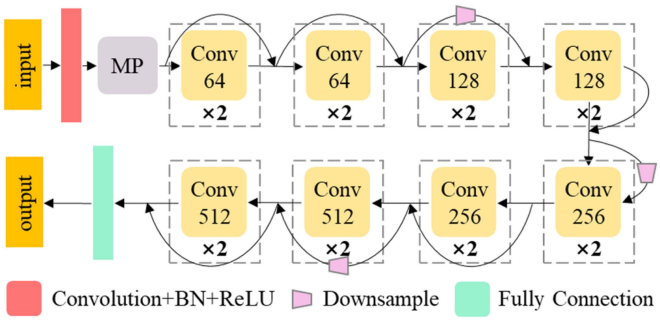

Fig. 5. Network structure of the ResNet18.

F. BisDeNet

Fig. 6 illustrates the specific structure of BisDeNet. In BisDeNet, DenseNet constructs a modular network for learning. The dense block (DB) in DenseNet is primarily used to create dense connections between the network layers. To maximize the information flow between all layers, DenseNet connects each layer with all its preceding layers. The input image first goes through a standard convolutional layer and then passes through four DBs with a transition layer (TL) added between each pair of adjacent DBs.

TL serves two purposes: reducing the output feature dimensions of the DB and avoiding excessive feature channel dimensions caused by concatenation operations. It simultaneously downsamples features to feed the next DB for further feature extraction. Based on this, BisDeNet efficiently extracts and refines landslide features with fewer parameters and lower computational costs. First, during backpropagation, each layer in DenseNet receives gradient signals from all its subsequent layers, ensuring that effective landslide features are learned as the network deepens. Second, the dual-branch CP is designed to obtain deep-level features and focus on the details of effective samples. By reusing features, DenseNet generates many landslide features using a small number of filters. In the CP of the dual-branch network, DenseNet acquires as many effective features as possible with relatively low computational costs. This approach reduces the model size while fully aggregating high-level semantic features.

G. Evaluation Metrics

Six commonly used EMs were selected to quantitatively evaluate the performance of the proposed network. These metrics include the overall accuracy (OA), precision (Pre), recall (Rec), $F1$-score ($F1$), Kappa coefficient (Kappa), and mean intersection over union (MIoU). These six EMs are defined as follows.

1) *OA*: Overall accuracy is one of the most common EMs and is typically defined as the proportion of correctly classified samples to the total number of samples. The formula for OA is shown in (3), where true positive (TP) and true negative (TN) refer to correctly predicted landslide samples and nonlandslide samples, respectively. False positive (FP) refers to the cases where the true value is nonlandslide, but the model incorrectly predicts the sample to be landslide. False negative (FN) refers to the cases where the true value is landslide, but the model incorrectly predicts the sample to be nonlandslide

$$\mathrm{OA} = \frac{\mathrm{TP}+\mathrm{TN}}{\mathrm{TP}+\mathrm{FP}+\mathrm{FN}+\mathrm{TN}}. \tag{3}$$

2) *Pre*: Precision refers to the proportion of correctly predicted landslide samples to all samples predicted as landslide samples. Pre is calculated as shown in the following equation:

$$\mathrm{Pre} = \frac{\mathrm{TP}}{\mathrm{TP}+\mathrm{FP}}. \tag{4}$$

3) *Rec*: Recall refers to the proportion of correctly predicted landslide samples to all actual landslide samples [see (5)]

$$\mathrm{Rec} = \frac{\mathrm{TP}}{\mathrm{TP}+\mathrm{FN}}. \tag{5}$$

4) *F1*: The $F1$-score is the harmonic mean of precision and recall. A higher $F1$-score indicates better performance of the model, and it is calculated as follows:

$$F1 = 2 \times \frac{\mathrm{Pre}\times\mathrm{Rec}}{\mathrm{Pre}+\mathrm{Rec}}. \tag{6}$$

5) *Kappa*: The Kappa coefficient is a comprehensive measure of classification accuracy that quantitatively evaluates the consistency between the classification results and the true labels. When its value is greater than 0.8, it indicates excellent consistency. The calculation of Kappa is

$$\mathrm{Kappa} = \frac{\mathrm{OA}-p_e}{1-p_e} \tag{7}$$

$$pe = \frac{(\mathrm{TP}+\mathrm{FN})(\mathrm{TP}+\mathrm{FP})+(\mathrm{FP}+\mathrm{TN})(\mathrm{FN}+\mathrm{TN})}{n^2}. \tag{8}$$

6) *MIoU*: The MIoU is calculated by first computing the intersection over union for each class in two sets and then taking their average. In semantic segmentation, these two sets represent the ground truth and the predicted values. In this study, the MIoU is calculated as follows:

$$\mathrm{MIoU} = \frac{1}{2}\left(\frac{\mathrm{TP}}{\mathrm{TP}+\mathrm{FN}+\mathrm{FP}}+\frac{\mathrm{TN}}{\mathrm{TN}+\mathrm{FN}+\mathrm{FP}}\right). \tag{9}$$

H. Landslide Dataset Construction and Parameter Setting

In this study, we randomly selected one landslide sample as the center in each of the two study areas and generated 1500 and 1000 sample patches of size 64 × 64. These patches were then divided into training data and validation data using a 3:7 ratio, with 30% used for training the DL model to learn landslide features and 70% used for evaluating the model's performance. Finally, the model was tested across the entire region to generate distribution maps of landslides in both study areas. To ensure that landslide boundaries were properly identified in the sample patches, we used a window with a size of 64 × 64 and a step size of 32. Data blocks of size $m \times n \times c$ were scanned from left to right and top to bottom in both study areas. As a result,

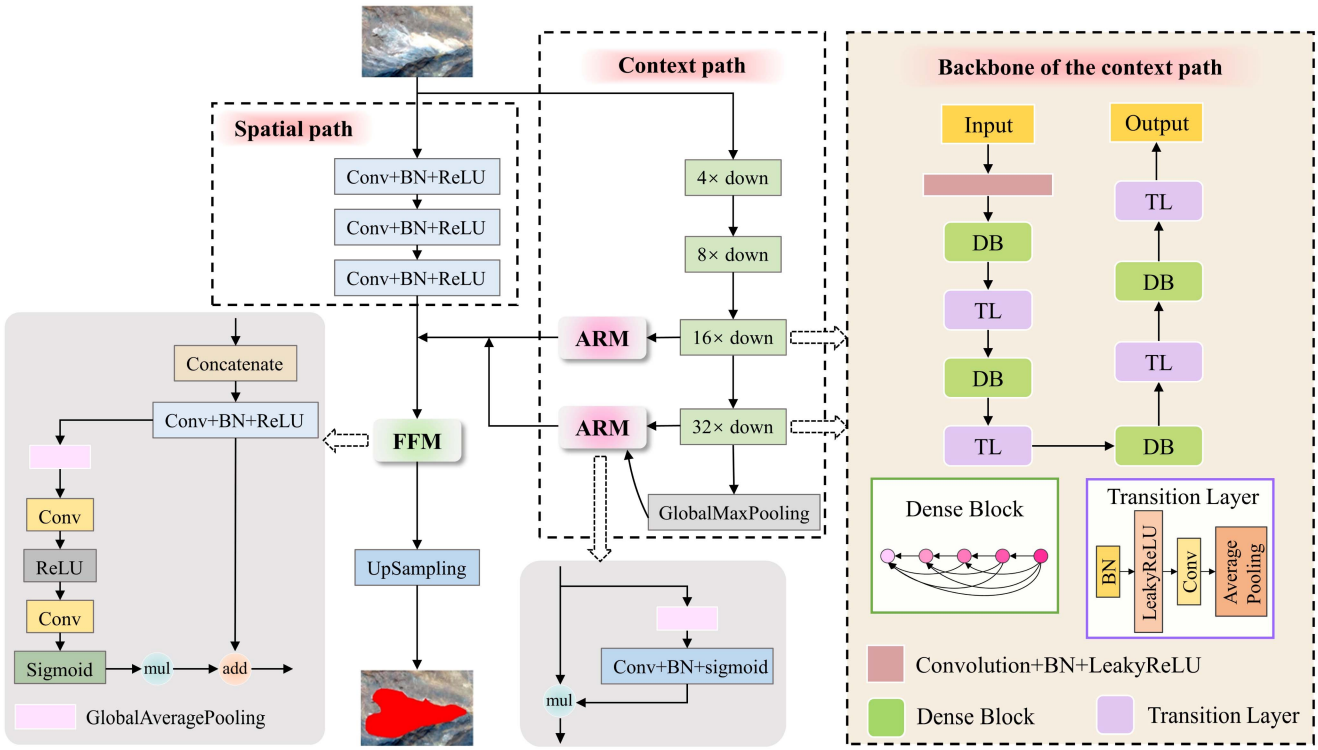

Fig. 6. Structure of the proposed BisDeNet.

TABLE II
COMPUTER HARDWARE INFORMATION

Item	Parameter
CPU	Intel Xeon(R) Silver 4210R CPU@2.4GHZ×40
GPU	GeForce RTX 3090/PCIe/SSE2
Memory	128GB
Hard disk	8TB

we generated 570 and 390 test sample patches in the two study areas for LD.

Table II presents the computer hardware utilized for the experiments in this study. The software was based on the Python 3.6 environment and built on the PyCharm 2021 software platform, and it was run on the Linux-Ubuntu 18.04.05 LTS operating system. The DL network was constructed using the Keras 2.2.0 artificial intelligence development framework.

The input image size was set to 64 × 64, and the network weights were initialized using random initialization. The LeakyReLU activation function with α set to 0.01 or 0 was used after the convolutional layers, and the sigmoid function was employed by the classifier at the end of the network. Since LD was treated as a binary classification problem in this study, the binary cross-entropy function was chosen as the loss function. To enhance feature extraction, dropout layers were added to the network, which randomly forgets a certain proportion of parameters during the training process, simplifying the model and avoiding vanishing gradients. The Adam optimizer was chosen for the network, with an initial learning rate usually set to 0.0001 or 0.001 and the batch size set to 2 for each learning iteration. The network was trained for 100 epochs, and the loss value on the validation set was monitored during training. When the loss value decreased, the *ModelCheckpoint* function saved the model. After the model was trained, the test dataset was input into the saved best-performing model for prediction, and the model generated the predicted image results.

IV. RESULTS AND ANALYSIS

A. Analysis of LCFs

1) Correlation Analysis of LCFs: Fig. 7(a) presents the visualization heatmap of the PCC for nine LCFs at Site 1. Darker colors represent stronger correlations, with positive/negative PCC values indicating positive/negative correlations. A few LCFs exhibit weak negative correlations, but most of them exhibit weak positive correlations. For example, elevation is positively correlated with slope, NDVI, and DTR, with correlation coefficients of 0.1225, 0.3929, and 0.5899, respectively. This suggests that in Site 1, locations closer to the river have lower elevations, while those farther away have higher elevations, and higher elevations correspond to steeper slopes and denser vegetation. On the other hand, MNDWI is negatively correlated with elevation and DTR, with correlation coefficients of −0.1801 and −0.183, respectively. This indicates that areas with higher elevations and greater DTRs have lower soil moisture contents. Overall, the correlations among these LCFs are not very strong. All correlation coefficients are below the critical value of 0.7, so no LCFs are eliminated in Site 1.

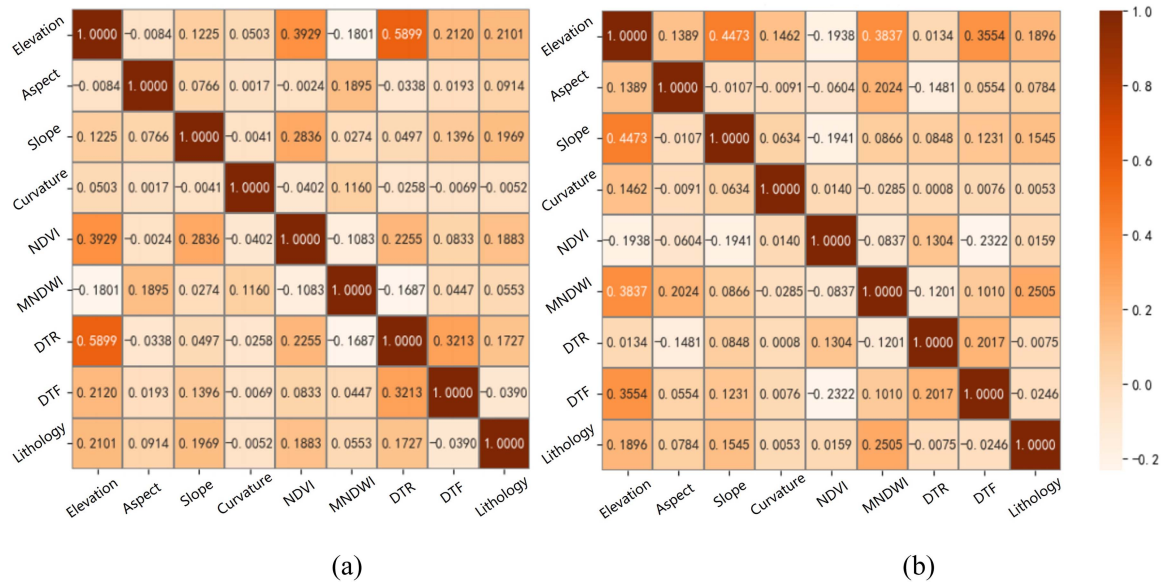

Fig. 7. Spearman correlation coefficients of LCFs. (a) Site 1. (b) Site 2.

TABLE III
MULTICOLLINEARITY TEST RESULTS OF LCFS IN TWO SITES

LCFs	Site 1		Site 2	
	VIF	TOL	VIF	TOL
Elevation	1.774	0.564	1.723	0.580
Aspect	1.049	0.953	1.073	0.932
Slope	1.145	0.873	1.325	0.754
Curvature	1.027	0.973	1.035	0.966
Lithology	1.131	0.884	1.104	0.906
DTF	1.172	0.853	1.279	0.782
NDVI	1.284	0.779	1.140	0.877
MNDWI	1.122	0.891	1.290	0.775
DTR	1.682	0.594	1.134	0.882

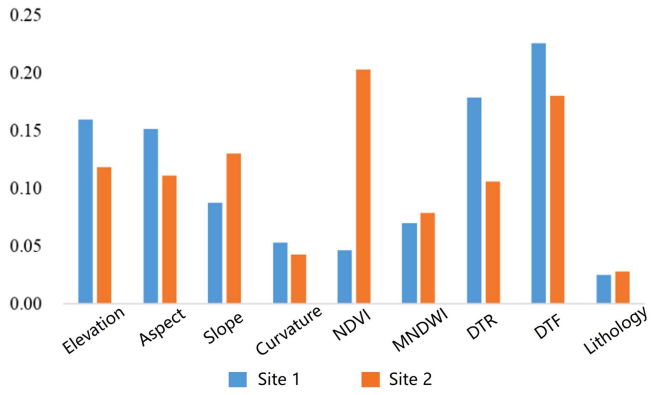

Fig. 8. Importance ranking results of LCFs in two sites.

Fig. 7(b) shows that, at Site 2, the slope is positively correlated with elevation and negatively correlated with NDVI, with correlation coefficients of 0.4473 and −0.1941, respectively. This indicates that higher elevations in the region correspond to steeper slopes and sparser vegetation. Similarly, the DTF is positively correlated with elevation and negatively correlated with NDVI, with correlation coefficients of 0.3554 and −0.2322, respectively. This indicates that areas farther from the fault have higher elevations and sparser vegetation. Additionally, areas with higher elevations also have higher soil moisture content. Since all the correlation coefficients among the LCFs, as shown in Fig. 5(b), are below the critical value of 0.7, no LCFs are eliminated in Site 2.

2) Multicollinearity Test of LCFs: Table III presents the VIF and TOL values of both sites. The TOL values of all LCFs in both sites are less than 5, so the LCFs have passed the multicollinearity test and do not need to be removed.

3) Importance Evaluation of LCFs: The importance ranking distribution of each LCF in the two sites is shown in Fig. 8. The DTF factor has the highest importance value at both sites because it is a triggering factor for landslides, whereas the lithology and curvature factors have low importance values, possibly due to their less significant variations. In Site 1, which consists mainly of rainfall-induced landslides, hydrological factors, such as DTR and MNDWI, are particularly important. However, the importance of these hydrological factors is not as pronounced in Site 2, where earthquake-induced landslides are more common. Additionally, at Site 1, many landslides are historical and stable, exhibiting new vegetation growth. As a result, the NDVI factor plays a minor role in the modeling process. In contrast, Site 2 has limited vegetation restoration activities due to its higher altitude and sparse vegetation, so the NDVI factor plays a more significant role in the modeling process. Finally, at both sites, factors related to terrain, such as elevation, slope, and aspect, are always crucial in identifying landslides because all landslides cause surface deformation.

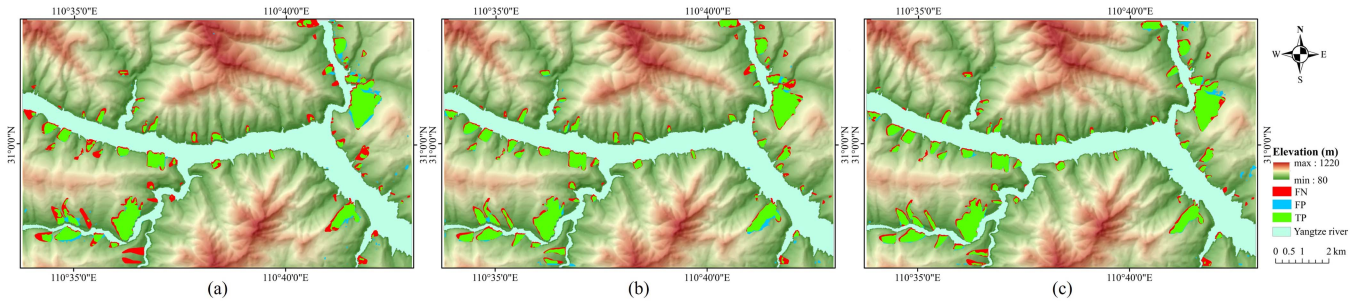

Fig. 9. Detection results of rainfall-induced landslides using three training datasets. (a) RS. (b) LCFs. (c) RSI-LCFs.

TABLE IV
EMs FOR DIFFERENT TRAINING DATASETS OF BISDENET AT SITE 1

Dataset \ EMs	OA	Pre	Rec	F1	Kappa	MIoU
RSI	0.9776	0.8696	0.7337	0.7959	0.7841	0.8188
LCFs	0.9876	0.9101	0.8789	0.8942	0.8877	0.8978
RSI-LCFs	**0.9883**	**0.9143**	**0.8872**	**0.9006**	**0.8944**	**0.9034**

(Bold and underlined values represent the optimal values of each EM).

TABLE V
EMs FOR DIFFERENT TRAINING DATASETS OF BISDENET AT SITE 2

Dataset \ EMs	OA	Pre	Rec	F1	Kappa	MIoU
RSI	0.9433	0.8101	0.7672	0.7880	0.7553	0.7934
LCFs	0.9573	0.8850	0.7923	0.8361	0.8116	0.8352
RSI-LCFs	**0.9694**	**0.9144**	**0.8574**	**0.8850**	**0.8674**	**0.8795**

(Bold and underlined values represent the optimal values of each EM).

B. Improvement of the LCFs on the Performance of BisDeNet

To explore the impact of LCFs on LD, we employ three distinct training datasets: RSIs, LCFs, and the combination of RSIs with LCFs (RSI-LCFs). These datasets are evaluated using the proposed BisDeNet model.

1) Site 1—Zigui County: Fig. 9(a)–(c) shows the results of LD at Site 1 using three different training datasets: RSI, LCFs, and RSI-LCFs. Visual inspection of the results reveals that the detection performance of Fig. 9(b) and (c) is superior to Fig. 9(a). Furthermore, the inclusion of LCFs leads to a more noticeable improvement in LD, particularly for small-scale landslides. Additionally, the boundary detection of landslides becomes more accurate and aligns better with the actual extent of the landslides. Moreover, it is evident that incorporating LCFs better distinguishes landslides from other similar features, significantly reducing the occurrence of misclassifying other features as landslides. Furthermore, comparing the identification results in Fig. 9(b) and (c), the visual differences are minimal. This might be attributed to the fact that most rainfall-induced landslides in the Three Gorges Reservoir area have already undergone gradual restoration, resulting in fewer discernible landslide features in the imagery.

Quantitative analysis of the detection results is presented in Table IV, showing the values of six EMs for LD using three different training datasets. It is evident that using RSI alone resulted in the lowest Rec of 73.37%. On the other hand, when utilizing only the LCFs, the Rec improved to 87.89%. However, when using the combined RSI-LCF dataset, the Rec reached an optimal value of 88.72%, indicating the critical importance of LCFs in LD for Site 1. Additionally, the inclusion of LCFs reduced the number of misidentified landslide pixels, demonstrating the utility of LCFs in distinguishing landslides from similar land cover types. In conclusion, the model trained with the RSI-LCFs dataset achieved the best results across all metrics. The $F1$, Kappa, and MIoU values reached their highest levels at 0.9006, 0.8944, and 0.9034, respectively. Although the improvement over using factors alone was only 0.64%, 0.67%, and 0.86%, it surpassed the performance of using imagery alone by 10.47%, 11.03%, and 8.46%, respectively.

2) Site 2—Jiuzhaigou County: The same comparative experiment was also verified in the earthquake-induced landslide area of Site 2. The causes and characteristics of landslides in this area are different from those in Site 1. Fig. 10 shows the detection results. It can be seen that, in this study area, Fig. 10(c) achieved the best detection results, while the results of Fig. 10(a) and (b) were not satisfactory. Both figures had too many landslides that were not identified and incorrectly identified. Fig. 10(a) had identification boundaries that did not match the actual landslide boundaries at all, whereas Fig. 10(b) model performed better in identifying boundaries for large landslides than Fig. 10(a). On the other hand, the model based on the RSI and LCFs, as shown in Fig. 10(c), accurately identified most of the landslides, including the boundaries and internal features of large landslides, as well as many small landslides. It also had minimal misidentification of other features as landslides, achieving satisfactory identification results. This is likely due to Site 2 being located in a higher altitude mountainous region with complex terrain and varying landslide sizes.

Table V presents the quantitative analysis of the detection results of different training samples for earthquake-induced landslides.

It can be observed that, similar to Site 1, when using only RSIs, all six EMs have the lowest values, even though the OA value reaches 0.9433. This is because the proportion of nonlandslide areas in the study area is very high, which increases the overall accuracy. The values of the Rec, $F1$, Kappa, and MIoU are all below 0.80 indicating that, when using only the RSI, many nonlandslide pixels are misclassified as landslides,

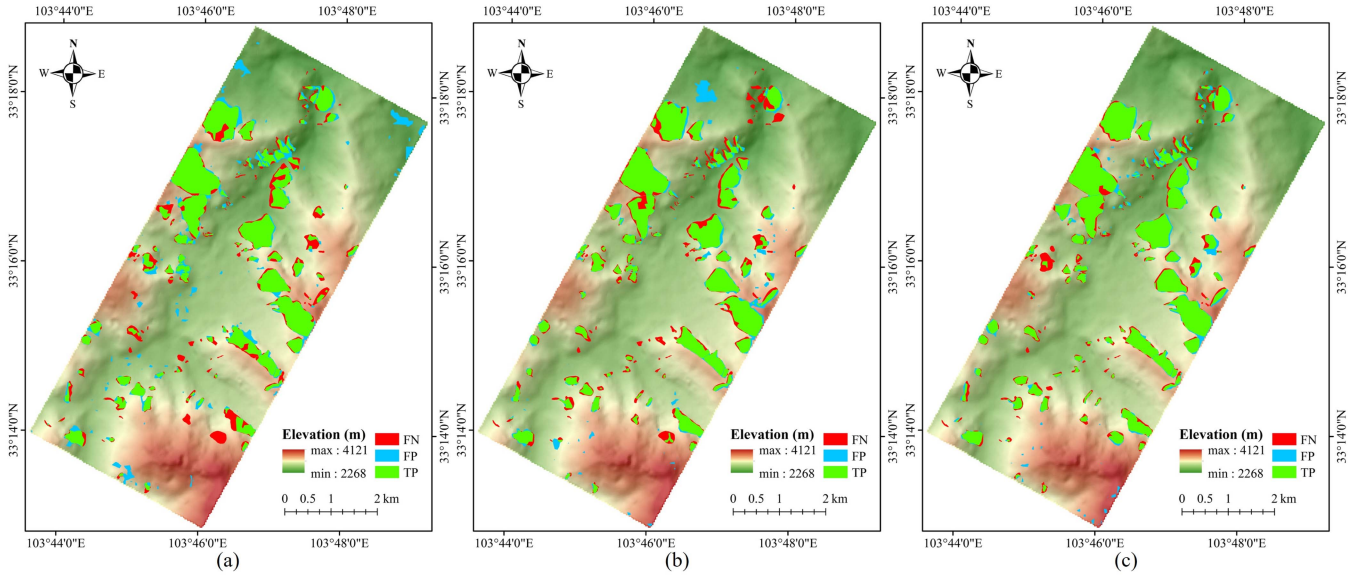

Fig. 10. Detection results of earthquake-induced landslides using three training datasets. (a) RS. (b) LCFs. (c) RSI-LCFs.

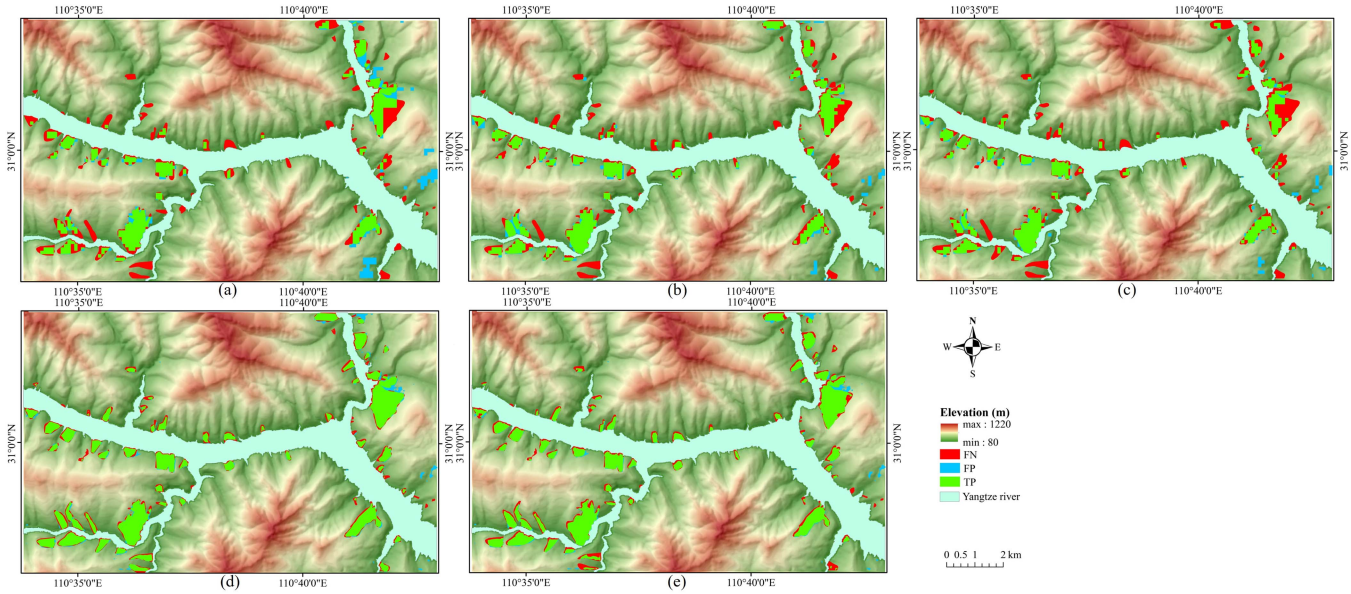

Fig. 11. LD results in Site 1. (a) BiSeNet. (b) BiSeNet-VGG. (c) BiSeNet-ResNet. (d) DeiT. (e) BisDeNet.

or some landslides are not correctly identified. However, when using only LCFs, all six EMs show improvement, suggesting that the landslide characteristics in Site 2 are more evident on the LCFs compared with the RSI. On the other hand, the model trained with RSI-LCFs as training data achieves the optimal results for all six EMs, indicating that the inclusion of LCFs has a positive effect on LD.

C. LD Results

In this section, the detection results of four lightweighted LD models (BiSeNet, BiSeNet-VGG, BiSeNet-ResNet, and BisDeNet), and advanced transformer-based methods, data-efficient image transformer (DeiT) [58], are analyzed and discussed.

1) Site 1—Zigui County: The detection results of the five lightweighted LD models at Site 1 are shown in Fig. 11. Specifically, Fig. 11(a), (b), (c), (d), and (e) depicts the LD results based on BiSeNet, BiSeNet-VGG, BiSeNet-ResNet, DeiT, and BisDeNet, respectively. BiSeNet, BiSeNet-VGG, and BiSeNet-ResNet perform poorly when identifying large landslides, such as the Kaziwan landslide, as their results significantly deviate from the actual landslide boundaries. However, they can better recognize medium-sized landslides, such as the Shuping

TABLE VI
EMs OF DIFFERENT MODELS AT SITE 1

EMs / Model	OA	Pre	Rec	F1	Kappa	MIoU
BiSeNet	0.9612	0.7153	0.5765	0.6384	0.6182	0.7143
BiSeNet-VGG	0.9700	0.8069	0.6517	0.7211	0.7054	0.7663
BiSeNet-ResNet	0.9670	0.8069	0.5863	0.6791	0.6622	0.7400
DeiT	0.9217	**0.9323**	**0.9217**	**0.9269**	0.8425	**0.9063**
BisDeNet	**0.9883**	0.9143	0.8872	0.9006	**0.8944**	0.9034

(Bold and underlined value means the highest EMs of the row).

TABLE VII
EMs OF DIFFERENT MODELS AT SITE 2

EMs / Model	OA	Pre	Rec	F1	Kappa	MIoU
BiSeNet	0.9442	0.8636	0.7052	0.7764	0.7449	0.7863
BiSeNet-VGG	0.9369	0.9021	0.6071	0.7258	0.6917	0.7504
BiSeNet-ResNet	0.9398	0.8824	0.6486	0.7477	0.7144	0.7655
DeiT	0.9333	**0.9412**	**0.9333**	**0.9372**	0.8660	**0.9303**
BisDeNet	**0.9694**	0.9144	0.8574	0.8850	**0.8674**	0.8795

(Bold and underlined value means the highest EMs of the row).

landslide, although many of these landslides were still not identified accurately. Moreover, these three models exhibit a considerable amount of overdetection, incorrectly classifying nonlandslide features with similar surface characteristics as landslides. This is attributed to the incomplete learning of semantic features by the network. Without parameter adjustments specific to LD, the performance of the BiSeNet model in particular is not satisfactory when the original method is directly applied. This indicates that certain differences exist between natural image classification tasks and LD tasks. Furthermore, when compared with BisDeNet, the LD results of the BiSeNet, BiSeNet-VGG, and BiSeNet-ResNet models exhibit pronounced jaggedness at the same spatial resolution. This can be attributed to the deeper network structure of these three models. The semantic paths in BiSeNet necessitate models with a reduced number of filters and heightened feature extraction capabilities for effective semantic feature extraction. The intricacy of the semantic paths in these three BiSeNet models proves to be too convoluted, resulting in a suboptimal extraction of landslide semantic features and, consequently, leading to rougher LD results. Additionally, from Fig. 11(d), it is evident that DeiT frequently overlooks the edge information of landslides.

Fig. 11(e) illustrates the LD results of the proposed BisDeNet model, which visually outperforms the other three models based on BiSeNet. From Fig. 11(e), it can be seen that most landslides are correctly identified, and their boundaries coincide with the actual ranges. The BisDeNet model also reduces misidentified landslides to a certain extent, which can significantly reduce the human labor, resource, and financial costs of practical rescue missions. However, a few landslides were not accurately identified. These landslides can be roughly categorized into two types: small-sized landslides and landslides located at the edge of the study area. This indicates that the model did not adequately learn the features of these types of landslides, which resulted in their failure to be identified during testing.

Table VI presents the six EMs of the five LD results at Site 1. Notably, the OA of the BisDeNet model attains the highest value, reaching 0.9883. Additionally, its Pre and Rec values are noteworthy, standing at 0.9143 and 0.8872, respectively, ranking as the second-highest values among the models. Furthermore, the BisDeNet model achieves the second $F1$, Kappa, and MIoU values of the five models, achieving values of 0.9006, 0.8944, and 0.9034, respectively. The Kappa coefficients are 27.62%, 18.90%, and 23.22% higher than those of BiSeNet, BiSeNet-VGG, and BiSeNet-ResNet, respectively. Moreover, except for the BisDeNet model, the other models do not reach $F1$, Kappa, and MIoU values of 0.8. This might be because the semantic paths of these three BiSeNet models are too complex, failing to effectively extract landslide semantic features. We also can see that DeiT achieves slightly better results than BisDeNet. However, it still encounters challenges associated with model size and a large number of parameters.

2) Site 2—Jiuzhaigou County: The five lightweight LD models were also applied for earthquake-induced LD at Site 2, yielding similar results (see Fig. 12). The three models, BiSeNet, BiSeNet-VGG, and BiSeNet-ResNet, can recognize only large-scale landslides in Site 2. Furthermore, their recognition of landslide boundaries appears grid-like and does not align well with the actual boundaries, resulting in poor continuity of the identified landforms. These models hardly detect medium and small landslides, especially those in lower altitude valley regions. This indicates that choosing inappropriate semantic path feature extraction frameworks considerably compromises the performance of BiSeNet.

However, the results of the BisDeNet model, constructed with only a few layers of DenseNet, appear visually superior to those of the first three models. BisDeNet can recognize all landslides within the study area, especially small landslides. Nevertheless, upon closer examination, the BisDeNet model exhibits some instances of both missed and false detections. This phenomenon is not widespread, occurring in only a few specific landslides. This is likely caused by the model's failure to learn the relevant features of such landslides during training due to insufficient representation of relevant information in the training samples. In Fig. 12(d), it is evident that the edges of landslides recognized by DeiT are not smooth and display a jagged appearance. This observation suggests that DeiT may not be well suited for the recognition of certain small landslides.

To quantitatively analyze and evaluate the earthquake-induced LD results in this region, six EMs for the models are provided (see Table VII). The Rec and Pre values of the BiSeNet model are 0.7052 and 0.8636, respectively. This model performs second only to the BisDeNet model, which exhibits Rec and Pre values of 0.9144 and 0.8574, respectively. On the other hand, the Rec and Pre of BiSeNet-VGG (0.6071 and 0.9021) and BiSeNet-ResNet (0.6486 and 0.8824) in this region are worse. Overall, BisDeNet demonstrates a relatively high level

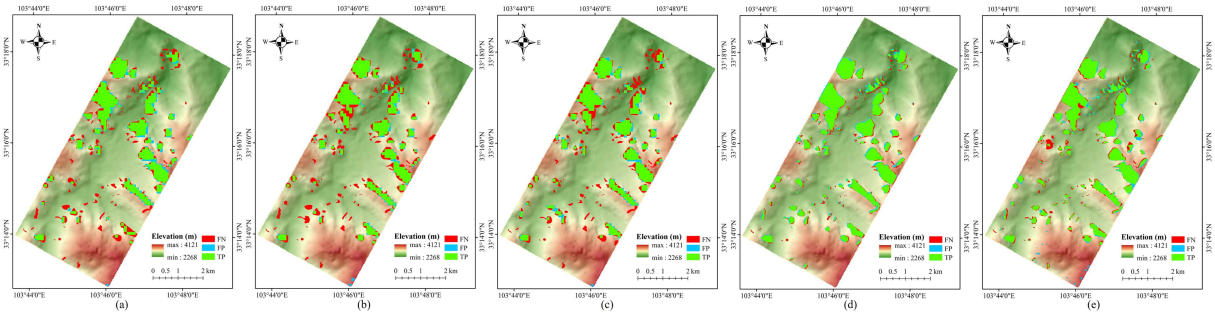

Fig. 12. LD results in Site 2. (a) BiSeNet. (b) BiSeNet-VGG. (c) BiSeNet-ResNet. (d) DeiT. (e) BisDeNet.

TABLE VIII
COMPARISON OF MODEL COMPLEXITY AND LEARNING EFFICIENCY

Models	Parameters	Model memory consumption (M)	Training Speed (ms/step)	Testing Speed (ms/step)
BiSeNet	26,563,486	305	134	21
BiSeNet-VGG	20,581,462	236	101	19
BiSeNet-ResNet	8,477,482	98	**66**	**10**
DeiT	22,901,226	272	207	35
BisDeNet	**467,523**	**7**	87	12

(Bold and underlined value means the highest EMs of the row).

of detection accuracy, with $F1$, Kappa, and MIoU values of 0.8850, 0.8674, and 0.8795, respectively. While these values are slightly lower than those of DeiT, BisDeNet achieves the highest OA and Kappa. This underscores its strong capability in effectively distinguishing landslides from the background, as visually demonstrated in the image representations. The corresponding values for the other three BiSeNet-based models are all below 0.8, indicating that the BisDeNet model's LD results are more consistent with the landslide labels than the results of the other models.

V. DISCUSSIONS

A. Efficiency of Different CPs on the Model Performance

Table VIII presents a comparison of the model parameters and model memory consumption of the five LD models. Bilateral semantic segmentation, which divides features into two pathways for extraction, employs distinct learning strategies. Furthermore, the attention optimization and FFMs do not increase the model's complexity, significantly enhancing the training and testing speeds of the model. Meanwhile, the BiSeNet, BiSeNet-VGG, and BiSeNet-ResNet models possess many parameters and have quite substantial sizes. In particular, BiSeNet, which employs the unmodified framework from the original BiSeNet article, is used directly for LD in this study. The Xception model used in BiSeNet extracts multiscale features by continually increasing the network width and depth, substantially increasing the complexity and decreasing the efficiency of the model. However, the fixed model architectures VGG and ResNet exhibit considerable depth, numerous filters, and intricate structures. However, a model with fewer filters and higher feature extraction capability is required for semantic feature extraction in BiSeNet's CP. Therefore, in this work, the DenseNet feature extraction component is ingeniously integrating into BiSeNet's CP, and the BisDeNet network model for LD is constructed. The BisDeNet model has the lowest parameter count of the models, just slightly over 460 000, and requires only 7 MB of memory. The training speed and testing speed are also comparatively fast, which effectively meets the requirements of landslide disaster response. It is worth mentioning that the training and testing speed of BisDeNet is slightly lower than that of BiSeNet-ResNet, as these speeds are influenced by various factors. There is not a direct causal relationship between the actual number of parameters and the training and testing speed. The number of parameters serves only as a reference for model training and testing. In comparison with BiSeNet-ResNet, BisDeNet exhibits lower computational density and a higher number of visits, resulting in marginally reduced training and testing speeds. Furthermore, when compared with DeiT, our proposed BisDeNet demonstrates clear advantages in terms of the number of parameters, model memory consumption, and speed. Remarkably, recognition accuracy does not show a substantial decrease, fully highlighting the excellent performance of BisDeNet.

B. Uncertainties in Lightweighted LD

While the BisDeNet network we introduced performed strongly in LD experiments across two sites, lightweight networks still encounter notable challenges within this field. Due to their smaller model capacity and reduced parameter count, lightweight networks exhibit lower model complexities. Consequently, these networks may struggle to capture the intricate textures and features of landslides present in RSIs, potentially resulting in diminished LD accuracy, particularly under complex terrains or varying weather conditions. Furthermore, lightweight networks may not perform strongly when applied across diverse geographical regions due to their sensitivity to parameter count. Lightweight networks may exhibit lower adaptability than nonlightweight networks to diverse landscapes and geological environments. Addressing these issues is imperative for enhancing the LD performance and reliability of lightweight networks.

C. Limitations and Future Work

In our work, we primarily focus on the streamline operation of the backbone network within the model architecture. This involves modifying feature extraction to attain a more lightweight network. Current model lightweightization methods include pruning, quantization, and knowledge distillation. Pruning reduces the model size by eliminating filters and channels, thereby decreasing the required storage space and computational resources and accelerating the network inference speed [59], [60]. Quantization employs fewer bits for representing model parameters, consequently reducing storage overhead [61], [62]. Knowledge distillation involves distilling knowledge from larger models to generate smaller submodels, compressing and accelerating the model [63], [64], [65].

In the future, conducting lightweightization work for LD using different model compression methods is plausible. Exploring combinations of various model compression techniques holds potential. Hybrid compression methods, which currently exist, have effectively balanced model accuracy and speed [66], [67]. Additionally, we will delve into the performance of existing lightweight networks, such as ShuffleNet and ENet. In our future work, a pivotal focus will be on integrating effective model compression methods for a comprehensive application to geological disaster issues. This allows LD tasks to be efficiently completed while accuracy is maintained, thereby facilitating landslide monitoring. Furthermore, it has been demonstrated that multimodal RS data and universal RS foundation model (SpectralGPT) can effectively improve the accuracy and generalization ability of semantic segmentation models, which brings great potential for further improvement of LD model performance [68], [69], [70].

VI. Conclusion

In this article, we introduce a novel lightweight DL framework named BisDeNet, designed to tackle the challenges of high model complexity in LD applications. We propose an improvement to the semantic segmentation network architecture by replacing the CPs in the original BiSeNet with DenseNet. This modification allows for the complete aggregation of high-level semantic features at a relatively low computational cost, thereby mitigating the computational burden associated with LD tasks. Through comprehensive qualitative and quantitative assessments of LD performance, we evaluate four lightweight semantic segmentation models along with an advanced transformer-based model across two distinct study areas: the Three Gorges Reservoir region and the Jiuzhaigou area. This study yields the following key findings.

1) By introducing simple yet effective modifications to both the spatial and context pathways of the BiSeNet model, our newly proposed BisDeNet consistently performs remarkably in both rainfall-induced landslide-prone regions within the Three Gorges Reservoir and postearthquake landslide-affected zones in Jiuzhaigou. This consistent performance across diverse geographical and geological conditions underscores the robust generalizability of BisDeNet.
2) The BisDeNet model exhibits a low parameter count and employs a densely connected architecture for robust feature extraction. This design choice contributes to the ability of the model to deliver satisfactory outcomes in lightweight LD tasks, demonstrating its efficiency in resource-constrained settings.

References

[1] M. Scaioni, L. Longoni, V. Melillo, and M. Papini, "Remote sensing for landslide investigations: An overview of recent achievements and perspectives," *Remote Sens.*, vol. 6, no. 10, pp. 9600–9652, Oct. 2014.

[2] C. Zhao, Z. Lu, Q. Zhang, and J. de La Fuente, "Large-area landslide detection and monitoring with ALOS/PALSAR imagery data over Northern California and Southern Oregon, USA," *Remote Sens. Environ.*, vol. 124, pp. 348–359, Sep. 2012.

[3] R. Hang, G. Li, M. Xue, C. Dong, and J. Wei, "Identifying oceanic eddy with an edge-enhanced multiscale convolutional network," *IEEE J. Sel. Topics Appl. Earth Observ. Remote Sens.*, vol. 15, pp. 9198–9207, Oct. 2022.

[4] R. Hang, X. Qian, and Q. Liu, "Cross-modality contrastive learning for hyperspectral image classification," *IEEE Trans. Geosci. Remote Sens.*, vol. 60, Jul. 2022, Art. no. 5532812.

[5] P. V. Gorsevski, M. K. Brown, K. Panter, C. M. Onasch, A. Simic, and J. Snyder, "Landslide detection and susceptibility mapping using LiDAR and an artificial neural network approach: A case study in the Cuyahoga Valley National Park, Ohio," *Landslides*, vol. 13, pp. 467–484, Jun. 2016.

[6] J. Barlow, Y. Martin, and S. E. Franklin, "Detecting translational landslide scars using segmentation of Landsat ETM+ and DEM data in the northern cascade mountains British Columbia," *Can. J. Remote Sens.*, vol. 29, no. 4, pp. 510–517, 2003.

[7] J. Dou et al., "Improved landslide assessment using support vector machine with bagging, boosting, and stacking ensemble machine learning framework in a mountainous watershed, Japan," *Landslides*, vol. 17, pp. 641–658, Mar. 2020.

[8] M. Marjanović, M. Kovačević, B. Bajat, and V. Voženílek, "Landslide susceptibility assessment using SVM machine learning algorithm," *Eng. Geol.*, vol. 123, no. 3, pp. 225–234, Nov. 2011.

[9] F. Catani, D. Lagomarsino, S. Segoni, and V. Tofani, "Landslide susceptibility estimation by random forests technique: Sensitivity and scaling issues," *Nature Hazards Earth Syst. Sci.*, vol. 13, no. 11, pp. 2815–2831, Nov. 2013.

[10] L. Ermini, F. Catani, and N. Casagli, "Artificial neural networks applied to landslide susceptibility assessment," *Geomorphology*, vol. 66, no. 1/4, pp. 327–343, Mar. 2005.

[11] T. Chen, J. C. Trinder, and R. Niu, "Object-oriented landslide mapping using ZY-3 satellite imagery, random forest and mathematical morphology, for the three-Gorges Reservoir, China," *Remote Sens.*, vol. 9, no. 4, Mar. 2017, Art. no. 333.

[12] F. Fiorucci et al., "Seasonal landslide mapping and estimation of landslide mobilization rates using aerial and satellite images," *Geomorphology*, vol. 129, no. 1/2, pp. 59–70, Jun. 2011.

[13] E. Maggiori, Y. Tarabalka, G. Charpiat, and P. Alliez, "Convolutional neural networks for large-scale remote-sensing image classification," *IEEE Trans. Geosci. Remote Sens.*, vol. 55, no. 2, pp. 645–657, Feb. 2017.

[14] Z. He, "Deep learning in image classification: A survey report," in *Proc. 2nd Int. Conf. Inf. Technol. Comput. Appl.*, 2020, pp. 174–177.

[15] R. Hang, P. Yang, F. Zhou, and Q. Liu, "Multiscale progressive segmentation network for high-resolution remote sensing imagery," *IEEE Trans. Geosci. Remote Sens.*, vol. 60, Sep. 2022, Art. no. 5412012.

[16] H. Cai, T. Chen, R. Niu, and A. Plaza, "Landslide detection using densely connected convolutional networks and environmental conditions," *IEEE J. Sel. Topics Appl. Earth Observ. Remote Sens.*, vol. 14, pp. 5235–5247, May 2021.

[17] X. Gao, T. Chen, R. Niu, and A. Plaza, "Recognition and mapping of landslide using a fully convolutional DenseNet and influencing factors," *IEEE J. Sel. Topics Appl. Earth Observ. Remote Sens.*, vol. 14, pp. 7881–7894, Aug. 2021.

[18] T. Liu, T. Chen, R. Niu, and A. Plaza, "Landslide detection mapping employing CNN, ResNet, and DenseNet in the three Gorges Reservoir, China," *IEEE J. Sel. Topics Appl. Earth Observ. Remote Sens.*, vol. 14, pp. 11417–11428, Oct. 2021.

[19] A. Ding, Q. Zhang, X. Zhou, and B. Dai, "Automatic recognition of landslide based on CNN and texture change detection," in *Proc. 31st Youth Academic Annu. Conf. Chin. Assoc. Autom.*, 2016, pp. 444–448.

[20] H. Yu, Y. Ma, L. Wang, Y. Zhai, and X. Wang, "A landslide intelligent detection method based on CNN and RSG_R," in *Proc. IEEE Int. Conf. Mechatronics Autom.*, 2017, pp. 40–44.

[21] O. Ghorbanzadeh, T. Blaschke, K. Gholamnia, S. R. Meena, D. Tiede, and J. Aryal, "Evaluation of different machine learning methods and deep-learning convolutional neural networks for landslide detection," *Remote Sens.*, vol. 11, no. 2, Jan. 2019, Art. no. 196.

[22] T. Lei, Y. Zhang, Z. Lv, S. Li, S. Liu, and A. K. Nandi, "Landslide inventory mapping from bitemporal images using deep convolutional neural networks," *IEEE Geosci. Remote Sens. Lett.*, vol. 16, no. 6, pp. 982–986, Jun. 2019.

[23] Y. Chen et al., "Susceptibility-guided landslide detection using fully convolutional neural network," *IEEE J. Sel. Topics Appl. Earth Observ. Remote Sens.*, vol. 16, pp. 998–1018, Dec. 2023.

[24] P. Liu, Y. Wei, Q. Wang, Y. Chen, and J. Xie, "Research on post-earthquake landslide extraction algorithm based on improved U-net model," *Remote Sens.*, vol. 12, no. 5, Feb. 2020, Art. no. 894.

[25] Z. Lu et al., "An iterative classification and semantic segmentation network for old landslide detection using high-resolution remote sensing images," *IEEE Trans. Geosci. Remote Sens.*, vol. 61, Sep. 2023, Art. no. 4408813.

[26] C. Fang, X. Fan, H. Zhong, L. Lombardo, H. Tanyas, and X. Wang, "A novel historical landslide detection approach based on LiDAR and lightweight attention U-net," *Remote Sens.*, vol. 14, no. 17, Sep. 2022, Art. no. 4357.

[27] X. Liu et al., "Feature-fusion segmentation network for landslide detection using high-resolution remote sensing images and digital elevation model data," *IEEE Trans. Geosci. Remote Sens.*, vol. 61, Jan. 2023, Art. no. 4500314.

[28] C. Niu, O. Gao, W. Lu, W. Liu, and T. Lai, "Reg-SA–UNet++: A lightweight landslide detection network based on single-temporal images captured postlandslide," *IEEE J. Sel. Topics Appl. Earth Observ. Remote Sens.*, vol. 15, pp. 9746–9759, Nov. 2022.

[29] Y. Yi and W. Zhang, "A new deep-learning-based approach for earthquake-triggered landslide detection from single-temporal RapidEye satellite imagery," *IEEE J. Sel. Topics Appl. Earth Observ. Remote Sens.*, vol. 13, pp. 6166–6176, Oct. 2020.

[30] B. Fang, G. Chen, L. Pan, R. Kou, and L. Wang, "GAN-based Siamese framework for landslide inventory mapping using bi-temporal optical remote sensing images," *IEEE Geosci. Remote Sens. Lett.*, vol. 18, no. 3, pp. 391–395, Mar. 2021.

[31] S. R. Meena et al., "Landslide detection in the Himalayas using machine learning algorithms and U-net," *Landslides*, vol. 19, no. 5, pp. 1209–1229, Feb. 2022.

[32] C. Q. Yu et al., "BiSeNet: Bilateral segmentation network for real-time semantic segmentation," in *Proc. Eur. Conf. Comput. Vis.*, 2018, pp. 334–349.

[33] S. Li, Q. Xu, M. Tang, and D. Zhu, "Study on spatial distribution and key influencing factors of landslides in three Gorges Reservoir area," *Earth Sci.*, vol. 45, no. 1, pp. 341–354, Jan. 2018.

[34] C. Xu et al., "A panorama of landslides triggered by the 8 August 2017 Jiuzhaigou, Sichuan Ms7.0 earthquake," *Dizhen Dizhi*, vol. 40, no. 1, pp. 232–260, Feb. 2018.

[35] J. Liu, T. Wang, J. Shi, and Z. Li, "Emergency rapid assessment of landslides induced by the Jiuzhaigou M_S 7.0 earthquake, Sichuan, China," *J. Geomech.*, vol. 23, no. 5, pp. 639–645, Oct. 2017.

[36] S.-B. Bai, J. Wang, G.-N. Lu, P.-G. Zhou, S.-S. Hou, and S.-N. Xu, "GIS-based logistic regression for landslide susceptibility mapping of the Zhongxian segment in the three gorges area, China," *Geomorphology*, vol. 115, no. 1/2, pp. 23–31, Feb. 2010.

[37] L. Peng, R. Niu, B. Huang, X. Wu, Y. Zhao, and R. Ye, "Landslide susceptibility mapping based on rough set theory and support vector machines: A case of the three gorges area, China," *Geomorphology*, vol. 204, pp. 287–301, Jan. 2014.

[38] K. Xu et al., "Landslide susceptibility evaluation based on BPNN and GIS: A case of Guojiaba in the three Gorges Reservoir area," *Int. J. Geograph. Inf. Sci.*, vol. 29, no. 7, pp. 1111–1124, Mar. 2015.

[39] K. Zhang, X. Wu, R. Niu, K. Yang, and L. Zhao, "The assessment of landslide susceptibility mapping using random forest and decision tree methods in the three Gorges Reservoir area, China," *Environ. Earth Sci.*, vol. 76, Jun. 2017, Art. no. 405.

[40] C. Zhou et al., "Landslide susceptibility modeling applying machine learning methods: A case study from Longju in the three Gorges Reservoir area, China," *Comput. Geosci.*, vol. 112, pp. 23–37, Mar. 2018.

[41] T. Chen, R. Niu, B. Du, and Y. Wang, "Landslide spatial susceptibility mapping by using GIS and remote sensing techniques: A case study in Zigui county, the three Georges Reservoir, China," *Environ. Earth Sci.*, vol. 73, no. 9, pp. 5571–5583, 2015.

[42] T. Chen, R. Niu, and X. Jia, "A comparison of information value and logistic regression models in landslide susceptibility mapping by using GIS," *Environ. Earth Sci.*, vol. 75, no. 10, May 2016, Art. no. 867.

[43] T. Chen, L. Zhu, R.-Q. Niu, C. J. Trinder, L. Peng, and T. Lei, "Mapping landslide susceptibility at the three Gorges Reservoir, China, using gradient boosting decision tree, random forest and information value models," *J. Mountain Sci.*, vol. 17, no. 3, pp. 670–685, Mar. 2020.

[44] L. Lv, T. Chen, J. Dou, and A. Plaza, "A hybrid ensemble-based deep-learning framework for landslide susceptibility mapping," *Int. J. Appl. Earth Observ. Geoinf.*, vol. 108, Apr. 2022, Art. no. 102713.

[45] W. Yu, Q. Gao, Y. Zhang, and S. Zhai, "Potential influencing factors analysis and safety evaluation on the landslide of high and steep slope," *Chin. J. Eng.*, vol. 30, no. 3, pp. 227–232, Mar. 2008.

[46] L.-C. Chen, G. Papandreou, I. Kokkinos, K. Murphy, and A. L. Yuille, "DeepLab: Semantic image segmentation with deep convolutional nets, atrous convolution, and fully connected CRFs," *IEEE Trans. Pattern Anal. Mach. Intell.*, vol. 40, no. 4, pp. 834–848, Apr. 2018.

[47] H. Zhao, J. Shi, X. Qi, X. Wang, and J. Jia, "Pyramid scene parsing network," in *Proc. IEEE Conf. Comput. Vis. Pattern Recognit.*, 2017, pp. 6230–6239.

[48] G. Huang, Z. Liu, L. Van Der Maaten, and K. Q. Weinberger, "Densely connected convolutional networks," in *Proc. IEEE Conf. Comput. Vis. Pattern Recognit.*, 2017, pp. 2261–2269.

[49] S. Jégou, M. Drozdzal, D. Vazquez, A. Romero, and Y. Bengio, "The one hundred layers tiramisu: Fully convolutional DenseNets for semantic segmentation," in *Proc. IEEE Conf. Comput. Vis. Pattern Recognit. Workshops*, 2017, pp. 1175–1183.

[50] K. He, X. Zhang, S. Ren, and J. Sun, "Deep residual learning for image recognition," in *Proc. IEEE/CVF Conf. Comput. Vis. Pattern Recognit.*, 2016, pp. 770–778.

[51] S. Ji, D. Yu, C. Shen, W. Li, and Q. Xu, "Landslide detection from an open satellite imagery and digital elevation model dataset using attention boosted convolutional neural networks," *Landslides*, vol. 17, pp. 1337–1352, Feb. 2020.

[52] A. Garcia-Garcia, S. Orts-Escolano, S. Oprea, V. Villena-Martinez, P. Martinez-Gonzalez, and J. Garcia-Rodriguez, "A survey on deep learning techniques for image and video semantic segmentation," *Appl. Soft Comput.*, vol. 70, pp. 41–65, Sep. 2018.

[53] S. D. Brown, "Introduction to multivariate statistical analysis in chemometrics," *Appl. Spectrosc.*, vol. 64, no. 4, Apr. 2010, Art. no. 112A.

[54] S. P. S. Gulick et al., "Importance of pre-impact crustal structure for the asymmetry of the Chicxulub impact crater," *Nature Geosci.*, vol. 1, no. 2, pp. 131–135, Jan. 2008.

[55] K. N. Berk, "Tolerance and condition in regression computations," *J. Amer. Statist. Assoc.*, vol. 72, no. 360, pp. 863–866, Dec. 1977.

[56] A. L. Boulesteix, A. Bender, J. L. Bermejo, and C. Strobl, "Random forest gini importance favours SNPs with large minor allele frequency: Impact, sources and recommendations," *Brief. Bioinform.*, vol. 13, no. 3, pp. 292–304, May 2012.

[57] K. Simonyan and A. Zisserman, "Very deep convolutional networks for large-scale image recognition," 2014, *arXiv:1409.1556*.

[58] H. Touvron, M. Cord, M. Douze, F. Massa, A. Sablayrolles, and H. Jégou, "Training data-efficient image transformers & distillation through attention," in *Proc. 38th Int. Conf. Mach. Learn.*, 2021, pp. 10347–10357.

[59] R. Yu et al., "NISP: Pruning networks using neuron importance score propagation," in *Proc. IEEE/CVF Conf. Comput. Vis. Pattern Recognit.*, 2018, pp. 9194–9203.

[60] C. Zhao, B. Ni, J. Zhang, Q. Zhao, W. Zhang, and Q. Tian, "Variational convolutional neural network pruning," in *Proc. IEEE/CVF Conf. Comput. Vis. Pattern Recognit.*, 2019, pp. 2775–2784.

[61] M. Rastegari, V. Ordonez, J. Redmon, and A. Farhadi, "XNOR-net: ImageNet classification using binary convolutional neural networks," in *Proc. Eur. Conf. Comput. Vis.*, 2016, pp. 525–542.

[62] B. Jacob et al., "Quantization and training of neural networks for efficient integer-arithmetic-only inference," in *Proc. IEEE/CVF Conf. Comput. Vis. Pattern Recognit.*, 2018, pp. 2704–2713.

[63] T. Nguyen, R. Novak, L. Xiao, and J. Lee, "Dataset distillation with infinitely wide convolutional networks," *Adv. Neural Inf. Process. Syst.*, vol. 34, pp. 5186–5198, 2021.
[64] P. Chen, S. Liu, H. Zhao, and J. Jia, "Distilling knowledge via knowledge review," in *Proc. IEEE/CVF Conf. Comput. Vis. Pattern Recognit.*, 2021, pp. 5006–5015.
[65] R. Huang and T. Chen, "Landslide recognition from multi-feature remote sensing data based on improved transformers," *Remote Sens.*, vol. 15, no. 13, Jun. 2023, Art. no. 3340.
[66] L. Yao, R. Pi, H. Xu, W. Zhang, Z. Li, and T. Zhang, "Joint-DetNAS: Upgrade your detector with NAS, pruning and dynamic distillation," in *Proc. IEEE/CVF Conf. Comput. Vis. Pattern Recognit.*, 2021, pp. 10170–10179.
[67] F. Tung and G. Mori, "Clip-Q: Deep network compression learning by in-parallel pruning-quantization," in *Proc. IEEE/CVF Conf. Comput. Vis. Pattern Recognit.*, 2018, pp. 7873–7882.
[68] D. Hong et al., "Cross-city matters: A multimodal remote sensing benchmark dataset for cross-city semantic segmentation using high-resolution domain adaptation networks," *Remote Sens. Environ.*, vol. 299, Dec. 2023, Art. no. 113856.
[69] D. Hong et al., "SpectralGPT: Spectral foundation model," 2023, *arXiv:2311.07113*.
[70] Y. Sun, Z. Fu, C. Sun, Y. Hu, and S. Zhang, "Deep multimodal fusion network for semantic segmentation using remote sensing image and LiDAR data," *IEEE Trans. Geosci. Remote Sens.*, vol. 60, Sep. 2022, Art. no. 5404418.

Tao Chen (Senior Member, IEEE) received the Ph.D. degree in photogrammetry and remote sensing from Wuhan University, Wuhan China, in 2008.

He is currently an Associate Professor with the School of Geophysics and Geomatics, China University of Geosciences, Wuhan, China. He has authored or coauthored more than 60 scientific papers, including IEEE TRANSACTIONS ON GEOSCIENCE AND REMOTE SENSING, IEEE JOURNAL OF SELECTED TOPICS IN APPLIED EARTH OBSERVATIONS AND REMOTE SENSING, *International Journal of Applied Earth Observation and Geoinformation*, etc., and guest-edited ten journal special issues. From 2015 to 2016, he was a Visiting Scholar with the University of New South Wales, Sydney, Australia. His research interests include image processing, machine learning, and geological remote sensing.

Dr. Chen serves as an Associate Editor for IEEE JOURNAL OF SELECTED TOPICS IN APPLIED EARTH OBSERVATIONS AND REMOTE SENSING.

Xiao Gao received the B.S. degree majoring in geographic information science from Henan University, Kaifeng, China, in 2019, and the M.S. degree majoring in geological resource and geological engineering from the China University of Geosciences, Wuhan, China, in 2022. She is currently working toward the Ph.D. degree in the discipline of surveying and mapping with Tongji University, Shanghai, China.

Her current main research interests include the variation and analysis of surface soil moisture in Qinghai–Tibet Plateau based on machine learning.

Gang Liu received the Ph.D. degree in cartography and geographic information engineering from Southwest Jiaotong University, Chengdu, China, in 2014.

He is currently a Professor with the College of Earth Sciences, Chengdu University of Technology, Chengdu, China. He has authored or coauthored more than 50 papers, including the *International Journal of Geographical Information Science*, *Transactions in GIS*, *Computers Environment and Urban Systems*, *Sustainable Cities and Society*, and *Journal of the Geological Society*. From 2018 to 2019, he was a Visiting Scholar with The University of Georgia, Athens, GA, USA. His research interests include spatial network, spatial analysis, geodata modeling, image interpretation, etc.

Chen Wang received the B.S. degree in geoinformation science and technology in 2021 from the China University of Geoscience, Wuhan, China, where she is currently working toward the M.S. degree in Earth exploration and information technology.

Her current research interests include the extraction of mine information from remote sensing imagery and deep learning methods for remote sensing image classification.

Zeyang Zhao received the B.S. degree majoring in geographic information science in 2021 from the Chengdu University of Technology, Chengdu, China, where he is currently working toward the M.S. degree in Earth exploration and information technology with the China University of Geosciences, Wuhan, China.

His current main research interests include landslide susceptibility mapping and deep learning.

Jie Dou received the Ph.D. degree in natural environmental studies from the University of Tokyo, Tokyo, Japan, in 2015.

He is a Full Professor with the China University of Geosciences, Wuhan, China. He extended his experience with the University of Tokyo, the Public Works Research Institute, etc. He has participated in research projects on earthquake/rainfall-triggered geohazards, spatial analysis with artificial intelligence, and risk mitigation. He got a Japan Society for the Promotion of Science fellowship. He has authored/coauthored more than 100 peer-reviewed articles.

Dr. Dou served as an Associate Editor for *Frontiers in Earth Science*, and on the editorial boards of several other international journals, such as the *Journal of Mountains Science*, *Geocarto International*, *Geomatics*, and *Natural Hazards and Risk*. He has besides served as a reviewer for more than 30 ISI-listed international journals. He has been a steering committee member of several commissions/working groups of international academic societies, such as the World Landslide Forum 5, BIGS2021, and BIGS2023.

Ruiqing Niu received the Ph.D. degree in Earth exploration and information technology from the China University of Geosciences, Wuhan, China, in 2005.

He is currently a Full Professor with the School of Geophysics and Geomatics, China University of Geosciences, Wuhan, China. His research interests include remote sensing, geographic information system, and engineering geology.

Antonio J. Plaza (Fellow, IEEE) received the M.Sc. and Ph.D. degrees in computer engineering from the Department of Technology of Computers and Communications, University of Extremadura, Badajoz, Spain, in 1999 and 2002, respectively.

He is currently a Full Professor and the Head of Hyperspectral Computing Laboratory, Department of Technology of Computers and Communications, University of Extremadura. He has authored more than 600 publications and guest-edited 10 journal special issues. He has reviewed more than 500 manuscripts for more than 50 different journals.

Dr. Plaza served as an Editor-in-Chief for IEEE TRANSACTIONS ON GEOSCIENCE AND REMOTE SENSING from 2013 to 2017. He is included in the Highly Cited Researchers List (Clarivate Analytics) from 2018 to 2020.